

Quantum properties near the instability boundary in optomechanical system

Han-Hao Fang(方晗昊), Zhi-Jiao Deng(邓志姣), Zhigang Zhu(朱志刚), and Yan-Li Zhou(周艳丽)
Citation: Chin. Phys. B, 2022, 31 (**3**): 030308. DOI: 10.1088/1674-1056/ac40f7
Journal homepage: http://cpb.iphy.ac.cn; http://iopscience.iop.org/cpb

What follows is a list of articles you may be interested in

Nearly invariant boundary entanglement in optomechanical systems

Shi-Wei Cui(崔世威), Zhi-Jiao Deng(邓志姣), Chun-Wang Wu(吴春旺), and Qing-Xia Meng(孟庆霞)
Chin. Phys. B, 2021, 30 (**11**): 110311. DOI: 10.1088/1674-1056/ac16ca

Tunable ponderomotive squeezing in an optomechanical system with two coupled resonators

Qin Wu(吴琴)
Chin. Phys. B, 2021, 30 (**2**): 020303. DOI: 10.1088/1674-1056/abb7f5

Generating Kerr nonlinearity with an engineered non-Markovian environment

Fei-Lei Xiong(熊飞雷), Wan-Li Yang(杨万里), Mang Feng(冯芒)
Chin. Phys. B, 2020, 29 (**4**): 040302. DOI: 10.1088/1674-1056/ab7741

Quantifying non-classical correlations under thermal effects in a double cavity optomechanical system

Mohamed Amazioug, Larbi Jebli, Mostafa Nassik, Nabil Habiballah
Chin. Phys. B, 2020, 29 (**2**): 020304. DOI: 10.1088/1674-1056/ab65b6

Controlling the entanglement of mechanical oscillators in composite optomechanical system

Jun Zhang(张俊), Qing-Xia Mu(穆青霞), Wen-Zhao Zhang(张闻钊)
Chin. Phys. B, 2018, 27 (**4**): 040304. DOI: 10.1088/1674-1056/27/4/040304

Quantum properties near the instability boundary in optomechanical system

Han-Hao Fang(方晗昊)[1,2], Zhi-Jiao Deng(邓志姣)[1,2,†], Zhigang Zhu(朱志刚)[3], and Yan-Li Zhou(周艳丽)[1,2]

[1] *Department of Physics, College of Liberal Arts and Sciences, National University of Defense Technology, Changsha* 410073, *China*
[2] *Interdisciplinary Center for Quantum Information, National University of Defense Technology, Changsha* 410073, *China*
[3] *Department of Physics, Lanzhou University of Technology, Lanzhou* 730050, *China*

(Received 18 September 2021; revised manuscript received 4 December 2021; accepted manuscript online 8 December 2021)

The properties of the system near the instability boundary are very sensitive to external disturbances, which is important for amplifying some physical effects or improving the sensing accuracy. In this paper, the quantum properties near the instability boundary in a simple optomechanical system have been studied by numerical simulation. Calculations show that the transitional region connecting the Gaussian states and the ring states when crossing the boundary is sometimes different from the region centered on the boundary line, but it is more essential. The change of the mechanical Wigner function in the transitional region directly reflects its bifurcation behavior in classical dynamics. Besides, quantum properties, such as mechanical second-order coherence function and optomechanical entanglement, can be used to judge the corresponding bifurcation types and estimate the parameter width and position of the transitional region. The non-Gaussian transitional states exhibit strong entanglement robustness, and the transitional region as a boundary ribbon can be expected to replace the original classical instability boundary line in future applications.

Keywords: optomechanical system, instability boundary, transitional region, quantum properties

PACS: 03.65.Ud, 42.65.Sf, 42.50.Wk **DOI:** 10.1088/1674-1056/ac40f7

1. Introduction

Optomechanical system,[1] which concerns the mutual interaction between radiation field and mechanical vibration, has received a lot of research interests. As the ground state cooling technology of the vibrator matures,[2,3] the study of the system's quantum properties at low temperatures becomes particularly important. One of the interesting parameter regions lies near the instability boundary, where the mechanical vibration evolves into self-sustained oscillation once crossing the boundary into unstable region.[1] Studies show that driving the system near the instability boundary would enhance the nonlinearity at single-photon level,[4] increase the quantum entanglement,[5] or exhibit divergent susceptibilities, which is good for quantum sensing.[6] Therefore, it is worthy to make clear its general quantum properties near the instability boundary.

In a previous work,[7] the common features, in particular the changing of quantum entanglement, while crossing the instability line by different parameter paths have been studied. Under the current situations of weak optomechanical coupling and strong laser driving in experiments,[8] the mean-field approximation[1] has to be adopted due to the huge intractable Hilbert space involved in solving master equation. The main idea is to assume small quantum fluctuations around the classical orbit represented by the mean values of quantum operators, and then do the standard linearization.[9,10] However, the results obtained have two limitations. One is that there is a tiny region close to the boundary where the fluctuations diverge,[7] and the other is that it ignores the system's non-Gaussian nature and can not show the characteristics of phase diffusion.[11]

The numerical solution of master equation can be possible in the single-photon strong coupling and weak driving regime,[12–16] where the optomechanical coupling strength is comparable to both the cavity decay rate and the mechanical frequency. Strong nonlinear effects such as photon blockade,[12] multiple sidebands in cavity output spectrum,[13] statistical mixture of two different oscillation amplitudes,[13,14] negative mechanical Wigner distribution,[15,16] sub-Poissonian mechanical states,[17] and Fano factor peak at phonon number threshold[18] have been discussed. But how are these nonlinear effects in parameter space related to the instability boundary, far away or nearby? Whether there are common features beyond the mean-field approximation when crossing the instability boundary?

The main purpose of this paper is to find out the general quantum properties near the instability boundary by numerical simulation of master equation. To do that, the system parameters should be adjusted to the regime of strong coupling and weak driving. Meanwhile, the classical orbits of mean values are depicted for comparison. The calculations show that while crossing the instability boundary from the stable region, the reduced mechanical state develops from Gaussian state to ring state with non-Gaussian transitional state connecting them. The Wigner distribution of transitional state directly re-

[†]Corresponding author. E-mail: dengzhijiao926@hotmail.com

© 2022 Chinese Physical Society and IOP Publishing Ltd

flects its bifurcation[19] behaviors in classical dynamics. There are typically two types: the supercritical Hopf bifurcation, and the saddle-node bifurcation followed by a subcritical Hopf bifurcation.[19] The transitional parameter region usually centers around the instability boundary, however, it might shift completely into the stable region where the saddle-node bifurcation takes place. In contrast to our initial intuitive, the transitional region instead of the vicinity of instability boundary is more fundamental. Its parameter width, position and bifurcation type can all be indicated by the mechanical second-order coherence function[20] and the optomechanical entanglement, and most importantly, the steady-state quantum entanglement in this region is very robust to thermal phonon noise. These results have revealed the general quantum features of optomechanical system near the instability boundary, many of which are missing in the mean-field approximation, thus also give some hints to rethink about the previous results[7] in the weak coupling regime.

The paper is organized as follows: In Section 2, after a brief review of the two-mode optomechanical system, the steady-state distribution on a two-dimensional stability diagram is presented. In Section 3, the transitional parameter region is focused for analysis, including its width and relative position to the instability boundary, two different types of bifurcations and their connection with mechanical Wigner distribution. The cross-boundary behaviors of the mechanical second-order coherence function and the optomechanical entanglement are discussed concretely in Section 4. Finally, the summary is given in Section 5.

2. Model and state distribution

The two-mode optomechanical system, which contains only one optical mode and one mechanical mode, has been studied thoroughly in many aspects.[1] Its Hamiltonian takes the following form in the rotating frame of driving laser frequency $\omega_{\rm L}$:[21]

$$\hat{H} = -\hbar\Delta\hat{a}^{\dagger}\hat{a} - \hbar g_0\hat{a}^{\dagger}\hat{a}\hat{q} + \frac{\hbar\omega_{\rm m}}{2}(\hat{q}^2+\hat{p}^2) + {\rm i}\hbar\Lambda(\hat{a}^{\dagger}-\hat{a}), \quad (1)$$

where $\Delta = \omega_{\rm L} - \omega_{\rm a}$ denotes the driving detuning with respect to cavity resonance, the driving amplitude is set by Λ, and the optomechanical coupling strength is g_0. The mechanical vibrator has eigenfrequency $\omega_{\rm m}$, and its dimensionless position and momentum are represented by operators $\hat{q} = (\hat{b}^{\dagger}+\hat{b})/\sqrt{2}$ and $\hat{p} = (\hat{b}-\hat{b}^{\dagger})/(\sqrt{2}{\rm i})$, respectively.

The complete system dynamics must include cavity photon loss and the Brownian noise acting on the mechanical vibrator. By averaging on both sides of quantum Heisenberg equations[22] to neglect noise terms and small quantum correlations, the set of classical dynamical equations described by the mean values of operators read[1]

$$\begin{aligned}\dot{a} &= ({\rm i}\Delta - \kappa/2)a + ig_0q_{\rm c}a + \Lambda,\\ \dot{q}_{\rm c} &= \omega_{\rm m}p_{\rm c},\\ \dot{p}_{\rm c} &= -\omega_{\rm m}q_{\rm c} + g_0|a|^2 - \gamma_{\rm m}p_{\rm c},\end{aligned} \quad (2)$$

with mean values $a \equiv \langle\hat{a}\rangle$, $q_{\rm c} \equiv \langle\hat{q}\rangle$, $p_{\rm c} \equiv \langle\hat{p}\rangle$, and $\gamma_{\rm m}$, κ denoting the mechanical damping rate and the cavity intensity decay rate respectively. The nonlinear dynamics of Eq. (2) has been widely studied including bistability,[23] limit cycles,[24] chaos,[25] etc. By letting all the first-order derivatives be zeros, the fixed points of this equation can be solved. The fixed point is stable (unstable) if it can attract (repel) any arbitrary close trajectories in phase space.[26] When driving the system with blue laser detuning ($\Delta > 0$) and large enough driving amplitude, the fixed point loses its stability to produce self-sustained mechanical oscillations,[14] and the vibrator undergoes periodic oscillation in the form $q_{\rm c} = q_0 + A\cos(\omega_{\rm m}t)$ with shifted equilibrium position q_0 and amplitude A. The instability boundary has been found by demanding that the total mechanical damping rate $\gamma_{\rm eff} = \gamma_{\rm m} + \gamma_{\rm opt} = 0$, with $\gamma_{\rm opt}$ being the optomechanical part induced by radiation pressure.[1] $\gamma_{\rm opt}$ can be positive or negative, which can either increase or decrease the total mechanical damping rate. In the blue-detuned regime, $\gamma_{\rm opt}$ is negative, decreasing the total damping rate. if $\gamma_{\rm eff} = \gamma_{\rm m} + \gamma_{\rm opt} < 0$, it can lead to amplification of thermal fluctuations and the system becomes unstable. So the boundary line approximately satisfies

$$\gamma_{\rm m} + \frac{g_0^2\Lambda^2\kappa}{2(\kappa^2/4+\Delta^2)} \times\left(\frac{1}{\kappa^2/4+(\Delta+\omega_{\rm m})^2} - \frac{1}{\kappa^2/4+(\Delta-\omega_{\rm m})^2}\right) = 0, \quad (3)$$

where $\gamma_{\rm opt}$ is the second term on the left side of the equation.

The quantum treatment of this open system can resort to the following Lindblad master equation:[1,20]

$$\dot{\hat{\rho}} = \frac{1}{{\rm i}\hbar}[\hat{H},\hat{\rho}] + \kappa\mathcal{D}[\hat{a}] + \gamma_{\rm m}(n_{\rm th}+1)\mathcal{D}[\hat{b}] + \gamma_{\rm m}n_{\rm th}\mathcal{D}[\hat{b}^{\dagger}], \quad (4)$$

where $\hat{\rho}$ is the density operator of the optomechanical system, $\mathcal{D}[\hat{o}] = \hat{o}\hat{\rho}\hat{o}^{\dagger} - (\hat{o}^{\dagger}\hat{o}\hat{\rho} + \hat{\rho}\hat{o}^{\dagger}\hat{o})/2$ is the standard Lindblad operator, and $n_{\rm th} = [\exp(\hbar\omega_{\rm m}/(k_{\rm B}T)) - 1]^{-1}$ is the mean thermal phonon number at temperature T. To make it in a solvable small truncated Hilbert space, the system parameters in Ref. [7] can be changed to reach the instability boundary with very low laser driving amplitude by such a way that, g_0 is increased and $\omega_{\rm m}$ is decreased by an order of magnitude respectively, and $\gamma_{\rm m}$ is reduced by three orders of magnitude. The maximum dimension of truncated Hilbert space in Fock-state basis $|l\rangle_{\rm opt}\otimes|n\rangle_{\rm mec}$ is about 4×350 or 3×500, which is manageable with QuTiP[27] on a computer server. The number of truncated phonons is increased to 380 or 520 respectively to test the convergence and the calculations remain unchanged, indicating that the number of truncated phonons is sufficient. The distribution probability on $|0\rangle_{\rm opt}$ exceeds 99%, while the

distribution probability on $|1\rangle_{\rm opt}$ or a higher state is on the order of 10^{-3} or even smaller. Therefore, the number of truncated photons is also sufficient.

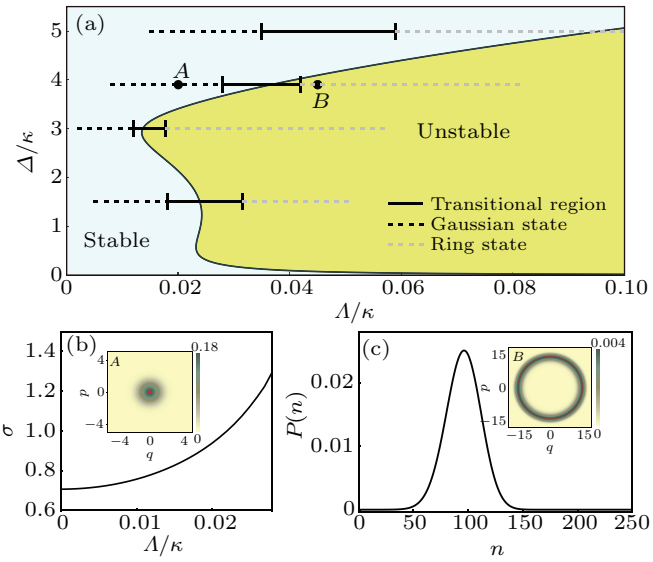


Fig. 1. (a) Steady-state distribution on a two-dimensional stability diagram according to the mechanical Wigner distribution, where parameters used are $g_0/\kappa = 0.5$, $\omega_{\rm m}/\kappa = 3$, and $\gamma_{\rm m}/\kappa = 10^{-5}$. The color division diagram of stability is the result of numerical calculation, while the black boundary curve is given by Eq. (3). Four horizontal paths that cross the boundary correspond to the drive detuning $\Delta/\kappa = 1.5$, 3, 3.9, 5 from bottom to top, respectively. Every path is divided into three regions: the solid black line represents the transitional region; the whole region on its left and right side is respectively Gaussian state (the dashed black line) and ring state (the dashed gray line). (b) Standard deviation σ of Gaussian states as a function of driving amplitude with $\Delta/\kappa = 3.9$. (c) Phonon number distribution for point B. The insets in panels (b) and (c) are the mechanical Wigner distributions for points A and B respectively, with their long-time classical orbits marked in red, the same marking for all the following Wigner functions.

Figure 1 shows the steady-state distribution on a two-dimensional stability diagram. Four representative cross-boundary paths were selected, including blue-sideband resonant driving at $\Delta = \omega_{\rm m}$ and cases where the amount of detuning is higher or lower than that. Especially we are interested in the mechanical Wigner distribution function $W_{\rm m}(q,p) = \frac{1}{\pi\hbar}\int_{-\infty}^{+\infty} dy\langle q+y|\hat{\rho}_{\rm m}|q-y\rangle\, {\rm e}^{2{\rm i}py/\hbar}$,[20] where $\hat{\rho}_{\rm m}$ is the reduced density matrix of mechanical vibrator after tracing out the optical degrees of freedom, q and p are the eigenvalues of operators $\hat{q}$ and $\hat{p}$, respectively. According to this quasi-probability distribution, the Gaussian states starting in stable region will evolve into ring states deep in the unstable region, with non-Gaussian transitional states connecting them. All of these states have rotational symmetry in phase space. The Gaussian state can be fitted with Gaussian function $W_{\rm Gaussian}(q,p) = \frac{1}{2\pi\sigma^2}\exp(-\frac{1}{2\sigma^2}(q^2+p^2))$. As the driving intensity increases, the standard deviation σ increases rapidly from $1/\sqrt{2}$ of the vacuum state without driving (see Fig. 1(b)). The ring state is defined as that its phonon number distribution function $P(n)$ has only a single peak and vanishes in the vicinity of $n = 0$. Usually, $P(n)$ is a symmetrical Gaussian function[18] as shown in Fig. 1(c), but when thermal phonon noise is considered, it might be distorted to be asymmetry. The width and position of the transitional region vary with parameters. Going up from $\Delta/\kappa = 3.9$, the transitional interval gradually goes from centering on the boundary line to completely leaving the boundary and entering the stable region.

3. Transitional region and bifurcations

This section mainly focuses on the change of the mechanical Wigner distribution function in the transitional region. To help understand these changes, the classical bifurcation behavior of the system is also given for comparison.

Figure 2 displays the change of quantum states in the transitional region under the blue-sideband resonant driving. Its classical bifurcation is a typical supercritical Hopf bifurcation,[19] where the stable fixed point loses stability and evolves into a stable limit cycle once crossing the instability boundary. The vibrator's amplitude A stays at zero in the stable region until it reaches the threshold $\Lambda_{\rm th}$ and starts to rise in proportional to $\sqrt{\Lambda - \Lambda_{\rm th}}$. The mechanical Wigner distribution just before the bifurcation at point C looks like a widened blob. For the three points D, E, and F after the bifurcation, the center of the blob will gradually sink as the blob becomes larger. The corresponding long-time classical trajectory marked in red shows that the quantum quasi-probability distribution is a broadening of the classical trajectory. Figure 2(b) compares the phonon number distributions of these four points. The peak for point C is located at $n = 0$, and then decreases while the peak gradually shifts to a larger phonon number. There is only one maximum in function $P(n)$.

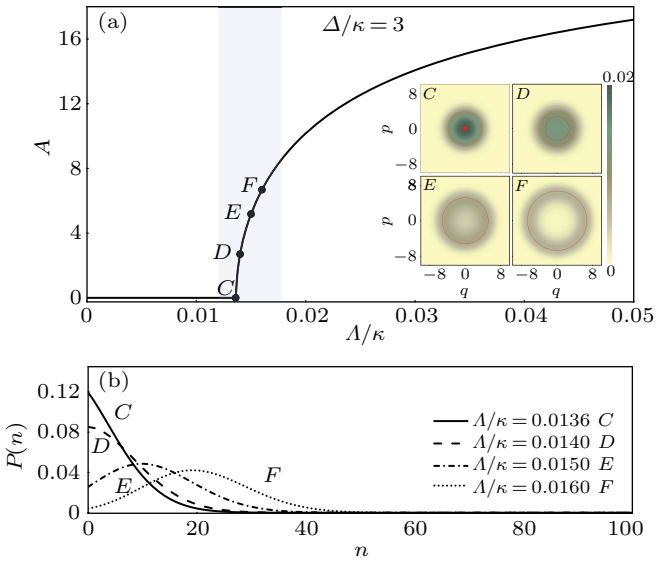


Fig. 2. (a) Changes in mechanical Wigner distribution in the transitional region with its corresponding bifurcation in the first type, where $\Delta/\kappa = 3$ and other parameters are the same as in Fig. 1. The transitional region is marked by the shaded part. (b) Comparison of phonon number distribution for points C, D, E, and F.

In order to clarify the influence of parameters on width

of the transitional region, the effect brought about by changing a certain parameter in Fig. 2 can be analyzed. The main results are demonstrated in Fig. 3. When the non-sideband resonant driving $\Delta/\kappa = 1.5$ is selected, the optomechanical interaction efficiency becomes weakened, the amplitude A rises relatively slowly, and the parameters that are farther away from the threshold point are required to form a ring state, so the width gets wider. When reducing the optomechanical coupling strength by 2.5 times to $g_0/\kappa = 0.2$, the threshold $\Lambda_{\rm th}$ will increase by 2.5 times, and the scale of amplitude A will also increase by 2.5 times, but the width of the noise will not increase by the same factor as the amplitude, which leads to a relatively smaller width of the transitional region. Point G corresponds to point F in Fig. 2. Its horizontal axis and vertical axis are both increased by 2.5 times, but it is in the ring state. If the mechanical damping rate is increased by 100 times to be $\gamma_{\rm m}/\kappa = 10^{-3}$, the threshold $\Lambda_{\rm th}$ will increase by 10 times. These two factors cancel each other to maintain the vibrator's amplitude scale and the noise width unchanged, so the relative width of the transitional region remains unchanged. Therefore, the key points to reduce the transitional width are to reduce the optomechanical coupling strength and select blue-sideband resonant driving.

In addition, when the amount of detuning Δ/κ is greater than 3.8, the feature of blob-annulus coexistence Wigner distribution appears in the quantum state transitional region. This is related to another two consecutive bifurcation behaviors.[19] First, a saddle-node bifurcation occurs in the stable region, which is accompanied by a transition from a single stable fixed point to an additional pair of stable and unstable limit cycles of almost equal size. As the driving amplitude continues to increase, the size of the stable limit cycle increases, while the size of the unstable limit cycle decreases. Until reaching the instability boundary, the unstable limit cycle merges with the stable point and a subcritical Hopf bifurcation occurs, which makes the stable point unstable, while the previous stable limit cycle remains. Between the two bifurcations is the coexistence interval of a stable fixed point and a stable limit cycle. The quantum and classical correspondences of this coexistence phenomenon are fuzzy when the amount of detuning is small. As an example in Fig. 4(a) with $\Delta/\kappa = 3.9$, point I is a coexistence parameter point in the classic description, but its mechanical Wigner distribution looks like a blob. Points J and K have only one stable limit cycle, but their $P(n)$ distributions have two extreme values, and there will be an obvious blob-annulus coexistence Wigner distribution between them.

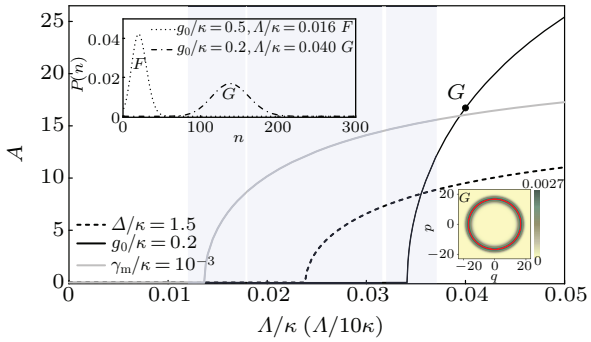


Fig. 3. Influence of parameters on width of the transitional region, with the same parameters as in Fig. 2 excepted the one marked in the plot. The bifurcation curve for $\gamma_{\rm m}/\kappa = 10^{-3}$ is rescaled 10 times smaller in the horizontal axis. The insets include the comparison of phonon number distribution for points F and G, and the mechanical Wigner distributions for point G.

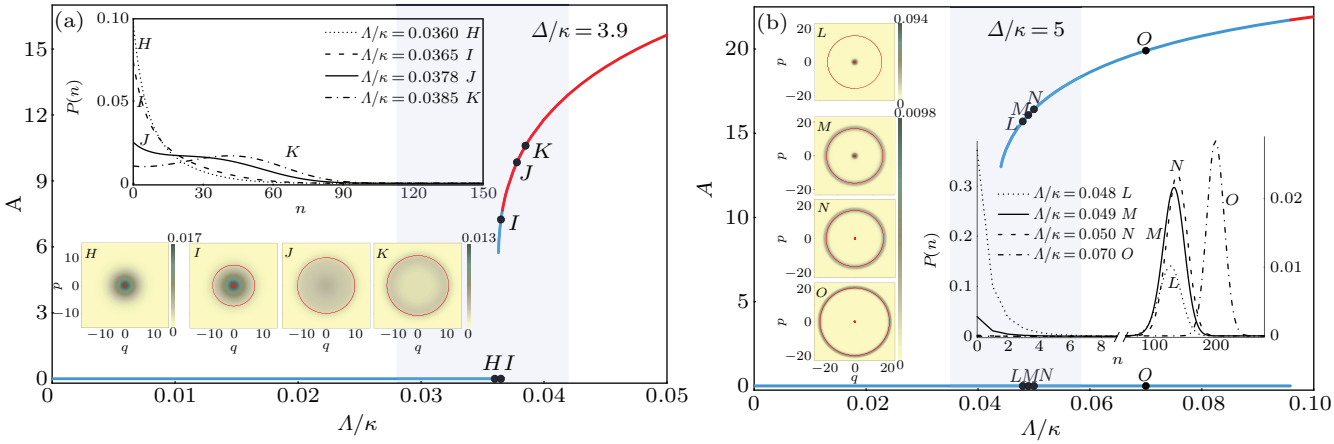


Fig. 4. Changes in mechanical Wigner distribution in the transitional region with its corresponding bifurcation in the second type, where $\Delta/\kappa = 3.9$ in (a) and $\Delta/\kappa = 5$ in (b) and other parameters are the same as in Fig. 1. The color of the bifurcation curve represents the stability of the fixed point, light blue indicates stable, and red indicates unstable in order to mark the instability boundary. Each panel has insets to show the phonon number distribution and mechanical Wigner distribution for four selected points.

When the driving detuning is increased, the classical coexistence interval increases significantly, and the quantum and classical descriptions have a very good correspondence. In Fig. 4(b) with $\Delta/\kappa = 5$, due to the relatively large size of the limit cycle in the first bifurcation, there are two completely independent peaks in $P(n)$ that are far apart, and their statistical weights shift from one to another quickly within a small parameter range. So the coexistence phenomenon in the Wigner

distribution only obviously occurs in a small range near the M point. In a large classical coexistence interval just before the instability boundary, the quantum states are completely in the ring states, such as the O point, whose $P(n)$ is a Gaussian distribution centered on $n \simeq 200$. Due to the statistical weight, the transitional region completely breaks away from the instability boundary and enters the stable region.

4. Indications of transitional region

The transitional region serves as an important link between the Gaussian states and the ring states. For different bifurcation behaviors, in addition to the different changes in the Wigner distribution function, what other quantum features will it have? This section mainly discusses the cross-boundary behavior of two physical quantities, i.e., the mechanical second-order coherence function and the optomechanical entanglement.

The mechanical second-order coherence function has the definition $g^{(2)}(0) = \frac{\langle \hat{b}^\dagger \hat{b}^\dagger \hat{b}\hat{b}\rangle}{\langle \hat{b}^\dagger \hat{b}\rangle^2} = 1 + \frac{V(n)-\langle \hat{n}\rangle}{\langle \hat{n}\rangle^2}$, with $V(n) = \langle \hat{n}^2\rangle - \langle \hat{n}\rangle^2$.[20] It reflects the distribution characteristics of the number of phonons, only related to the diagonal elements of the mechanical reduced density matrix even if there are non-zero off-diagonal matrix elements. Figure 5 shows the change of $g^{(2)}(0)$ under two different bifurcation behaviors. Figures 5(a) and 5(b) behave the same on both sides except for the transitional region. When the mean thermal phonon number $n_{\rm th} = 0$, the vibrator starts in a vacuum state without driving, and $g^{(2)}(0)$ near it has divergence. While if $n_{\rm th} \neq 0$, the vibrator starts from the thermal state with $g^{(2)}(0) = 2$. In the ring state region, $g^{(2)}(0)$ is close to 1 due to amplitude noise suppression for limit cycles, and it even has a weak sub-Poisson distribution with $g^{(2)}(0)$ slightly smaller than 1 for $n_{\rm th} = 0$.[17] The divergence of $g^{(2)}(0)$ can be explained within a small truncated Hilbert space. At weak driving, most of the population is on state $|0\rangle_{\rm opt}|0\rangle_{\rm mec}$, and the states it can reach are $|1\rangle_{\rm opt}|n\rangle_{\rm mec}$ with $n = 0, 1, 2$. Using the perturbation method to expand up to Λ^2, the result $g^{(2)}(0) \propto 1/\Lambda^2$ can be obtained. The divergence of $g^{(2)}(0)$ can also be explained from the diagonal elements of the mechanical reduced density matrix, which is very close to the vacuum state at weak driving. The phonon numbers variance $V(n)$ and expectation value $\langle \hat{n}\rangle$ of the vacuum state are both zeros, so $g^{(2)}(0)$ is divergent. When the number of mean thermal phonons is tiny (less than 1×10^{-2}), there is an approximate expression $g^{(2)}(0) \approx 2\rho_{33}/\rho_{22}^2$, where ρ_{22} and ρ_{33} are the second and third diagonal matrix elements of the mechanical density matrix respectively. Although ρ_{33} is so tiny, it differs from the third diagonal matrix element of the corresponding thermal state by one or two orders of magnitude. This difference makes the value of the mechanical second-order correlation function not equal to 2 ($g^{(2)}(0)$ of the thermal state), but a larger value. As the number of mean thermal phonons increases, the mechanical diagonal matrix elements are exactly the same as those of the thermal state, so $g^{(2)}(0)$ is equal to 2.

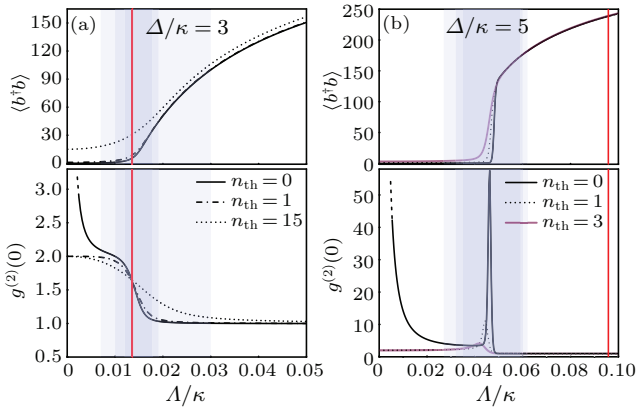


Fig. 5. Cross-boundary behavior of the mechanical second-order coherence function for two different bifurcation types, where $\Delta/\kappa = 3$ in (a) for the first type and $\Delta/\kappa = 5$ in (b) for the second type, and other parameters are the same as in Fig. 1. The overlapping shaded parts indicate multiple transitional regions. The larger the number of mean thermal phonons, the wider the transitional region. Red lines indicate the instability boundary.

In the transitional region, different bifurcations correspond to different changes in $g^{(2)}(0)$. For the first type of bifurcation, $g^{(2)}(0)$ decreases monotonically from a value close to 2 to close to 1. The parameter width of the transitional interval just corresponds to $g^{(2)}(0)$ in this value range. As the number of mean thermal phonon $n_{\rm th}$ increases, the transitional interval widens, and the curve of $g^{(2)}(0)$ becomes gentler (see Fig. 5(a)). For the second type of bifurcation, due to the rapid transfer of statistical weight between the two peaks, the number of phonons increases sharply after the first saddle-node bifurcation as shown in Fig. 5(b). At the low end of the rising edge of the phonon number, there is a spike corresponding to $g^{(2)}(0)$, where the phonon number is small, but its variance increases significantly due to the two-peak structure, thus leading to a maximum. Along the rising edge, $g^{(2)}(0)$ drops rapidly because of the significant increase in the number of phonons. When $n_{\rm th}$ is increased, the weight of the small right peak in function $P(n)$ can be increased, so the rising edge of the number of phonons shifts to the left, while the peak value of $g^{(2)}(0)$ shifts to the left and decreases. This is also accompanied by a widening of the transitional region and its center position shifting to the left.

The optomechanical entanglement, i.e., the entanglement between optical and mechanical modes, is also generated in this system due to the two-mode squeezing term in the Hamiltonian.[1] In the previous work,[7] the entanglement in the unstable region restricted by the mean-field approximation always oscillates with time, and the entanglement characteristics in the non-Gaussian steady state cannot be obtained. Here, the non-Gaussian case could be discussed by numerical

simulations. The entanglement measure utilized is the logarithmic negativity, which is defined as $E_{\rm N} = \log_2 \left\|\rho^{\rm T_A}\right\|_1$ with $\left\|\rho^{\rm T_A}\right\|_1$ being the trace norm of the partial transpose of density matrix ρ.[28] Figure 6(a) shows the change of steady-state entanglement across the instability boundary at resonant sideband driving. For $n_{\rm th} = 0$, the entanglement increases rapidly from zero to form a single peak and then falls near the instability boundary, and then increases approximately linearly. This single peak is the competition result of enhanced interaction caused by increased driving and the enlarged noise as it gets closer to the boundary. The rising process of entanglement under weak driving can be well approximated by the perturbation treatment in a small truncated Hilbert space. The slope and the height of the peak depend on the optomechanical coupling strength and the mechanical damping rates as shown in Fig. 6(a). By decreasing g_0/κ and increasing $\gamma_{\rm m}/\kappa$, this single peak will disappear and the entanglement increase monotonically approaching the instability boundary, in consistent with the previous weak coupling results.[7]

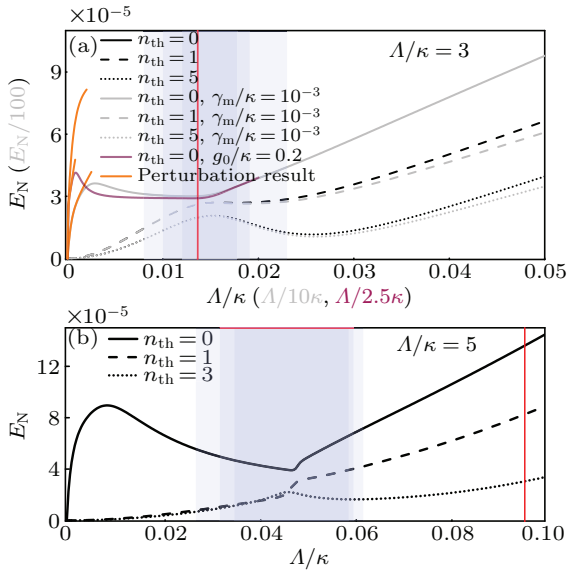


Fig. 6. Cross-boundary behavior of optomechanical entanglement for two different bifurcation types, where $\Delta/\kappa = 3$ in (a) for the first type and $\Delta/\kappa = 5$ in (b) for the second type, and other parameters are the same as in Fig. 1. The extra gray curves in (a) give the results after $\gamma_{\rm m}/\kappa$ is increased by 100 times, their horizontal axis is reduced by 10 times, and vertical axis is reduced by 100 times for comparison. Another additional purple curve in (a) gives the result for decreasing g_0/κ by 2.5 times, only its horizontal axis is reduced by 2.5 times for comparison. The oranges curves for $n_{\rm th} = 0$ are obtained by the perturbation treatment in a small truncated Hilbert space, where photon numbers are $\{0, 1\}$, and phonon numbers are $\{0, 1, 2\}$, and expanding up to Λ^2 terms. The overlapping shaded parts indicate multiple transitional regions with $g_0/\kappa = 0.5$, $\omega_{\rm m}/\kappa = 3$, and $\gamma_{\rm m}/\kappa = 10^{-5}$ for different mean thermal phonon numbers. Red lines indicate the instability boundary with these parameters and the zoomed instability boundary with g_0/κ or $\gamma_{\rm m}/\kappa$ changed.

When considering the influence of thermal phonon noise, the entanglement under weak driving decreases rapidly, and the entanglement in the ring state region also decreases significantly, but it still maintains a linear increase trend. The least affected is the transitional region, where the entanglement changes from a local minimum to a local maximum. As mentioned above, increasing $\gamma_{\rm m}/\kappa$ by 100 times only enlarges the horizontal axis by 10 times, and the relative width and position of the transitional region remain unchanged. What's more interesting is that the entanglement is only correspondingly increased by 100 times, and the changing curves with different $\gamma_{\rm m}/\kappa$ are very similar or even completely coincident (see Fig. 6(a)). The entanglement curves corresponding to the second type of bifurcation are depicted in Fig. 6(b). The outcomes are very similar, except that the entanglement in the transitional region has more subtle phenomena such as two bends and steps, anyhow, the entanglement in this region is also very robust to thermal phonon noise. For the weak coupling case, this entanglement robustness has also been found around the instability boundary.[7] It can be inferred that as the strength of optomechanical coupling increases, attention should be paid to the transitional region, which might be different from the region centered on the boundary line.

5. Conclusion

To summarize, the general quantum properties in a two-mode optomechanical system near the instability boundary have been investigated by numerical simulations. According to the mechanical Wigner distribution, Gaussian states starting from the stable region will gradually evolve to the ring states deep in the unstable region after passing through a transitional region. The change of the mechanical Wigner distribution in the transitional region directly reflects its bifurcation behavior in classical dynamics. Besides, the cross-boundary behaviors of quantum properties such as mechanical second-order coherence function, and optomechanical entanglement, are all closely related to the corresponding classical bifurcations. In turn, these quantum properties can be used to judge the corresponding bifurcation types and estimate the parameter width and position of the transitional region. For example, if a spike suddenly appears in the $g^{(2)}(0)$ function, it signifies that the saddle-node bifurcation in the second type of bifurcation has occurred, and the transitional region is an interval centered on this spike. The statistical weight also plays an import role, which might make the transitional region differ from the region centered on the boundary line. The former is more essential than the latter and its entanglement is very robust to thermal phonon noise, which are out of our previous expectation. In future applications, the transitional region should replace the instability boundary as the starting point for analysis and research.

Acknowledgements

Z. J. Deng is grateful to Liang Huang, Qiong-Yi He, Jie-Qiao Liao and Xiao-Bo Yan for useful discussions. This

work is supported by the National Natural Science Foundation of China (Grant Nos. 11574398, 12174448, 12174447, 11904402, 12074433, 11871472, and 12004430).

References

[1] Aspelmeyer M, Kippenberg T J and Marquardt F 2014 *Rev. Mod. Phys.* **86** 1391
[2] Qiu L, Shomroni I, Seidler P and Kippenberg T J 2020 *Phys. Rev. Lett.* **124** 173601
[3] Liu Y C, Hu Y W, Wong C W and Xiao Y F 2013 *Chin. Phys. B* **22** 114213
[4] Xu X, Gullans M and Taylor J M 2015 *Phys. Rev. A* **91** 013818
[5] Deng Z J, Habraken S J M and Marquardt F 2016 *New J. Phys.* **18** 063022
[6] Dutta S and Cooper N R 2019 *Phys. Rev. Lett.* **123** 250401
[7] Meng Q X, Deng Z J, Zhu Z G and Huang L 2020 *Phys. Rev. A* **101** 023838
[8] Peterson G A, Kotler S, Lecocq F, Cicak K, Jin X Y, Simmonds R W, Aumentado J and Teufel J D 2019 *Phys. Rev. Lett.* **123** 247701
[9] Wang G, Huang L, Lai Y C and Grebogi C 2014 *Phys. Rev. Lett.* **112** 110406
[10] Zhang D and Zheng Q 2013 *Chin. Phys. Lett.* **30** 024213
[11] Li W, Piergentili P, Li J, Zippilli S, Natali R, Malossi N, Giuseppe G D and Vitali D 2020 *Phys. Rev. A* **101** 013802
[12] Rabl P 2011 *Phys. Rev. Lett.* **107** 063601
[13] Nunnenkamp A, B crkje K and Girvin S M 2011 *Phys. Rev. Lett.* **107** 063602
[14] Ludwig M, Kubala B and Marquardt F 2008 *New J. Phys.* **10** 095013
[15] Qian J, Clerk A A, Hammerer K and Marquardt F 2012 *Phys. Rev. Lett.* **109** 253601
[16] Nation P D 2013 *Phys. Rev. A* **88** 053828
[17] Rodrigues D A and Armour A D 2010 *Phys. Rev. Lett.* **104** 053601
[18] Armour A D and Rodrigues D A 2012 *C. R. Physique* **13** 440
[19] Crawford J D 1991 *Rev. Mod. Phys.* **63** 991
[20] Walls D F and Milburn G J 2008 *Quantum Optics*, 2nd Ed. (Berlin: Springer-Verlag) pp. 38–42
[21] Law C K 1995 *Phys. Rev. A* **51** 2537
[22] Gardiner C W and Collett M J 1985 *Phys. Rev. A* **31** 3761
[23] Aldana S, Bruder C and Nunnenkamp A 2013 *Phys. Rev. A* **88** 043826
[24] Marquardt F, Harris J G E and Girvin S M 2006 *Phys. Rev. Lett.* **96** 103901
[25] Bakemeier L, Alvermann A and Fehske H 2015 *Phys. Rev. Lett.* **114** 013601
[26] Strogatz S H 1994 *Nonlinear Dynamics and Chaos* (Cambridge: Perseus Publishing) pp. 18–26
[27] Johansson J R, Nation P D and Nori F 2013 *Comp. Phys. Comm.* **184** 1234
[28] Vidal G and Werner R F 2002 *Phys. Rev. A* **65** 032314